Evolution in microstructure and compression behaviour of a metallic sintered friction material after braking

I. Serrano-Munoz, J. Rapontchombo, Vincent Magnier, F. Brunel, S. Kossman, P. Dufrénoy

Available online at www.sciencedirect.com
ScienceDirect
(2019) –18
Journal Logo

Evolution in microstructure and compression behaviour of a metallic sintered friction material after braking

I. Serrano-Munoz[a,b,*], J. Rapontchombo[b], V. Magnier[b], F. Brunel[b], S. Kossman[c], P. Dufrénoy[b,*]

[a]*Current address: Bundesanstalt für Materialforschung und -prüfung (BAM), Unter den Eichen 87, 12205, Berlin, Germany*
[b]*Univ. Lille, CNRS FRE 2016 - LaMcube - Laboratoire de Mécanique, Multiphysique, Multiéchelle, F-59000 Lille, France*
[c]*Arts et Métiers ParisTech, MSMP, Lille 59800, France*

Abstract

Due to the complexity of friction materials, the characterization of the tribological properties is prioritised over the bulk material properties even though the tribology is expected to be influenced by the material behaviour. The extent of this relationship is still unknown and further knowledge is required to account for the load history and evolution of the bulk properties. With this view, the compression behaviour and microstructure of a semi-metallic friction material with reduced formulation were investigated before and after a braking program. The thermal loading was monitored with inserted thermocouples. Uniaxial compression tests coupled with Digital Image Correlation (DIC) show significant changes in the worn material, which develops a compression behaviour similar to that of a tri-layered material. The microstructural analysis indicates microcracking and carbon diffusion in the Fe-phase. The thermal loading was found to be the key parameter controlling both the friction behaviour and evolution of the material properties. The expected effects of material evolution on the contact uniformity, durability and tribology are discussed.

Keywords: Semi-metallic sintered material, Braking load history, Uniaxial compression tests, Digital image correlation, DIC, Scanning Electron Microscopy, SEM, Evolution of bulk properties

1. Introduction

Friction materials are at the heart of defining the performance of braking systems. Because these materials are crucial to the transportation safety, they have to fulfil numerous requirements involving different fields: a constant level of friction whatever the conditions of use to ensure the stopping distance, a low rate of wear to decrease the life-cycle costs, high mechanical strength for integrity, and limited noise and vibration, just to name a few. The extensive requirements have led to the development of very complex materials containing many different component types [1, 2]. The use of a metal-matrix composite (MMC) is needed to withstand the high temperature due the dissipation of very high energies (*e.g.,* in the railway industry). In addition, fillers (*e.g.,* ceramic and graphite particles) need to be added to fulfil the wear and friction requirements. In the past, this complexity (material and conditions of use) has led to empirical developments mostly reliant on trial-error iterations.

The investigation of the friction level and wear rates along with the characterization of the contact surface (usually limited to a depth of ~100 μm) provides knowledge of some key mechanisms involved in the tribology. It has been reported that the material immediately beneath the contact surface (sub-surface material) has a significant influence

*Corresponding authors:
Email addresses: itziar.serrano.munoz@gmail.com (I. Serrano-Munoz), philippe.dufrenoy@polytech-lille.fr (P. Dufrénoy)

on the mechanisms controlling the generation of wear sources (*e.g.,* erosion, cracks or hot-spots) [2**?** –9]. Regarding the bulk properties, the studies published to date mainly focus on the mechanisms involved in disc cracking. For cast-iron [10, 11] and steel [12–15] materials, it was shown that the cracking is induced by phase transformations occurring during the braking. In [14, 15], the transformation from austenite to martensite/bainite is observed in steel discs that endured cycles of high thermal loading (800-1200°C) followed by rapid cooling. On the other hand, very few studies deal with the evolution of the friction material facing the disc [7, 16]. In particular, reference [16] reported a strong modification in the mechanical properties of a semi-metallic material after a high-energy braking sequence was applied (*e.g.,* the stiffness decreased from 5,800 MPa in the virgin material to 1,100 MPa in the worn one).

The above studies indicate that the evolution of friction materials during braking has a multilevel nature (*i.e.,* changes in the bulk and subsurface affect the contact surface). The further advancement of friction materials requires in-depth understanding of how the evolution in bulk properties influences the braking performance. The present study approaches the challenge by investigating the mechanisms involved in the evolution of the compression behaviour. Moreover, a detailed characterization of the mechanical properties will lead to more realistic numerical simulations, ultimately contributing to a reduction in the empirical dependency of the braking-process simulations. The usefulness of thermomechanical modelling is shown, for example, in references [16–22]. These studies used numerical simulations to investigate the influence of brake-pad design on the development of contact pressure localisations and subsequent formation of hot spots.

Given that the multi-loading and multi-physics nature of the braking process generally obscures the elucidation of mechanisms, the present study utilizes a sintered friction material with reduced formulation (only nine components) and the mechanical characterization is limited to uniaxial compression tests. The braking program is carried out using a real-scale dynamometer, where the temperature level of the friction material is monitored with inserted thermocouples. The friction behaviour and differences in compressive properties and microstructure are examined. The mechanisms involved in the evolution of the compression behaviour are discussed along with the expected influence of these mechanisms on the braking performance.

2. Material and methods

2.1. Material

The *simplified* formulation (reduced to *only* nine components) is given in Table 1. This material can be considered as a (FeCu-based) metal matrix composite that contains particles of graphite, ceramics and a small percentage of fillers and lubricant particles, which are included in the metallic matrix percentage.

Main Components	**Mass (%)**	**Size**
Metallic Matrix (MM)	70	Sintering powder <100 μm
Graphites 1 & 2	20	100-600 μm 400-1100 μm
Ceramics 1 & 2	10	100-200 μm 100-250 μm

Table 1. Friction material composition.

The manufacturing process consists of three main steps: (i) preparation of the raw powders, including weighing and mixing, (ii) compacting of the powders (up to 1,000 tons along the Z axis) using a shaped mould to consolidate the and densify the model (also known as green compact), and (iii) sintering in a protective-atmosphere furnace for 8h at ~1,000°C. The final dimensions of the brake-pad is surface = 200 cm^2 and height = 22.5 mm. Note that the compacting and in-service loads are applied along the same direction .

The wide range in the size of particles leads to a complex multiscale material. As shown in Fig. 1a, only Graphite 2 particles can be observed at a macroscopic scale length (*i.e.,* with the naked eye). In addition to Graphite 2 particles, Graphite 1 (also shown in black but with smaller sizes) and the ceramic particles are distinguishable at the mesoscale (Fig. 1b). Finally, the two principal phases of the metallic matrix (ferrite iron and copper) can be observed at the microscopic scale length (Fig. 1c-d). Note that some pearlite colonies are observed in Fig. 1c-d. These colonies

most probably result from the diffusion of carbon, which has originated from the graphite particles, into the Fe matrix during the sintering process.

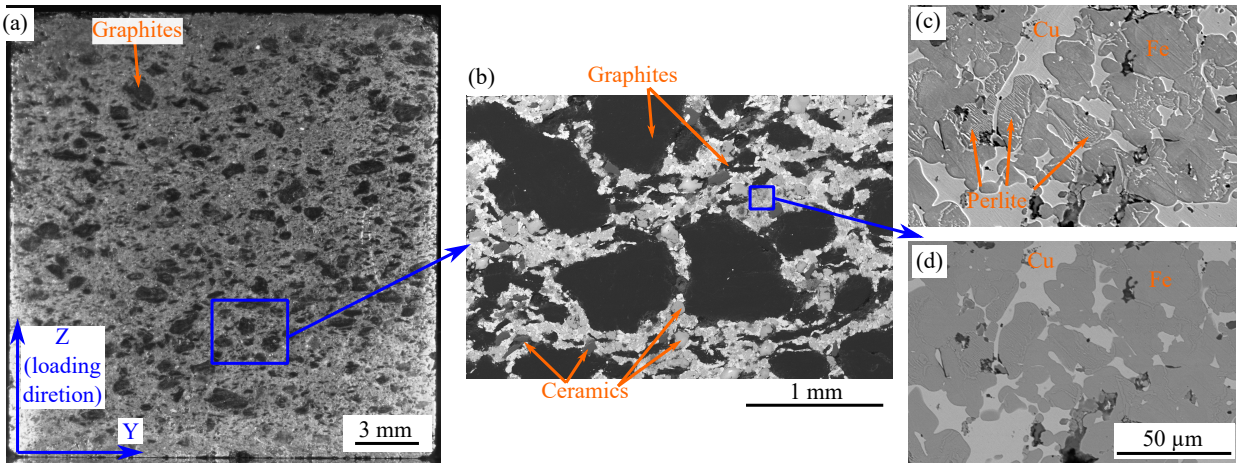

Figure 1. Microstructure of the studied friction material: (a) Light-optical image at the macroscopic scale length. (b) Backscattered Electron (BSE) image at the mesoscopic scale length (c) Secondary Electron (SE) image of the metallic matrix at the microscopic scale length and (d) same as previous image but in BSE mode. Here, the pearlite colonies are almost indistinguishable. The surface was etched with Nital reagent for 5 s.

The density of the virgin material was measured using the Archimedes method, which compares the sample weight when measured in dry air and saturated in ethanol, giving information about the open porosity. For the studied material, the porosity content is 14% (mass percentage). Synchrotron Computed Tomography (SCT, carried out at ID19 beamline of the European Synchrotron Radiation Facility (ESRF), Grenoble, France) was performed to gain qualitative knowledge about the porosity. The investigated sample was a cylinder 5 mm in diameter and 18 mm in height (where the height is parallel to the compression direction). The scanning was performed at 110 KeV with a voxel size of 3.425 μm^3. The images were reconstructed from projections by applying Paganin's phase retrieval algorithm [23] and subsequent filtered back-projection reconstruction for parallel beam. The SCT images correspond to the mesoscopic scale length.

In the reconstructed images (Fig. 2a), the two types of graphite particles and Ceramic 1 particles exhibit similar dark-grey levels. Ceramic 2 particles are shown in light-grey and the metallic matrix is close to white (grey-scale values of 220-255). Close observation of the graphite particles indicates that these particles contain some crack-like intrinsic porosity (Fig. 2b). It is likely that the intra-porosity only occurs within Graphite 2 particles, as this type of porosity is not observed within the smallest Graphite 1 particles. The SCT images also show some interface-porosity (considered as a discontinuity, Fig. 2c) between the metallic matrix and the graphite/ceramic particles, as well as between individual graphite/ceramic particles. It is, therefore, probable that the porosity distribution throughout this friction material is complex and heterogeneous. Moreover, it is likely that this mesoscale porosity only accounts for a portion of the 14% measured by the Archimedes method. Nevertheless, a detailed study of the nanoporosity content within the metallic matrix is outside of the scope of this study.

2.2. *Methods*

2.2.1. *Braking set-up and protocol*

A real-scale railway dynamometer, replicating those used in TGV high-speed trains, was used to apply realistic braking loads to the friction pair. It was equipped with a solid disc (non-ventilated) made of a 28CrMoV5 steel (Fig. 3a) and brake pads made of the friction material described in Section 2.1. The brake pads and disc were brought into contact by a pneumatic caliper actuated with a pressure-control system. In addition to the standard output data usually acquired during typical laboratory experiments (*e.g.,* actuator pressure, torque and rotation speed), thermal monitoring was carried out to record the temperatures induced in the friction pair. The pad thermocouples were inserted from the back side of each brake pad at two different depths (3 and 6 mm, measured from the virgin contact surface). The thermocouple locations are shown in Fig. 3b. Regarding the disc, three rubbing thermocouples were

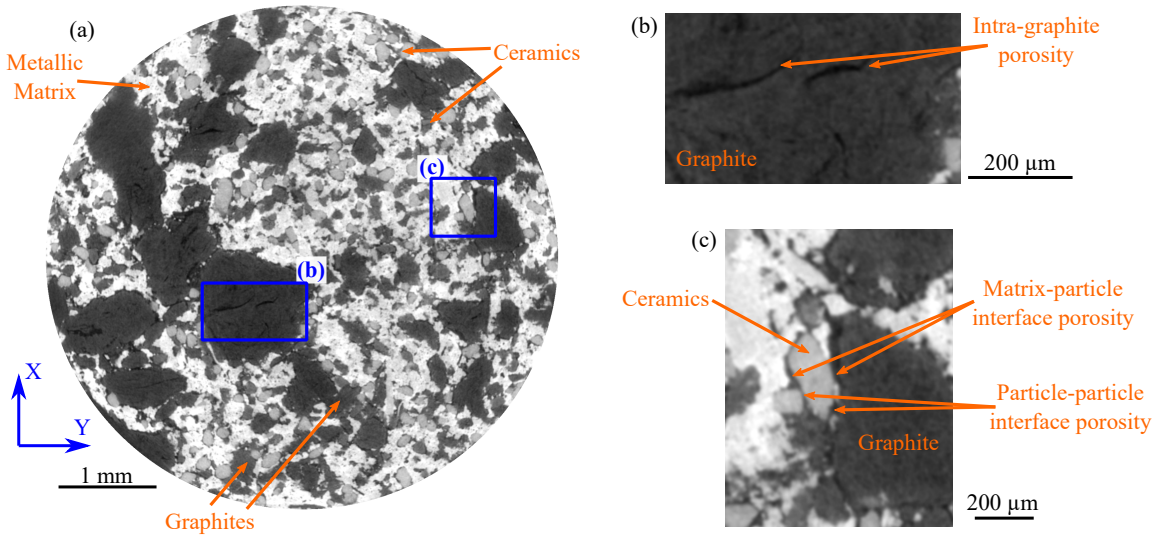

Figure 2. (a) 2D slice (transverse plane) of the reconstructed synchrotron CT data corresponding to the material mesoscopic scale length. (b) Detail of a Graphite 2 particle showing some intrinsic porosity. (c) Detail of the metallic matrix, where the porosity/discontinuity between the matrix and the graphite/ceramics particles in addition to some porosity at the interface between individual graphite/ceramic particles can be observed.

used (see Fig. 3a) as well as an infrared camera located in front of the disc surface to record the occurrence of thermal localisations.

The test program was specifically designed to investigate the level of thermal loading induced by an increasing energy dissipation during braking and follows the guidelines of the Union Internationale des Chemins de fer (UIC, International Union of Railways is the translation in English). An initial S0 braking sequence, not noted in Fig. 3c, was performed prior to the program. This initial braking was performed with the same normal force used in S1V0. Once 80% of the contact surface was worn away by friction (the verification was done visually), the program shown in Fig. 3c was started. This braking program consisted of three blocks (series) of low, medium and high braking energy (S1, S2 and S3). The increment in braking energy was achieved by increasing the inertial mass to be stopped (see fifth column in Fig. 3c). The braking force applied on the pad (defined as normal force in Fig. 3c) was also increased in each series. Before the starting of each series, five low-energy braking sequences were carried out as a breaking-in procedure, meant to resettle the contact surfaces for the following series. These series were subdivided into five braking sequences, where the speed (equivalent to the speed of an in-service train) was progressively increased. Each braking sequence is noted as S(i)V(i).

2.2.2. *Uniaxial compression tests*

Compression tests required the extraction of cubic samples (~20×20×20 mm^3, a volume considered large enough to be representative of the macroscopic behaviour) from the central region of the brake pad (see Fig. 4a). A testing machine equipped with a 50 kN load cell was used with a loading rate of 0.01 mm/s. The loading/unloading direction corresponds to the in-service braking direction. No important barrelling effects were observed during the experiments and, therefore, the cross section dimension was kept constant at 20×20 mm^2. The top and bottom surfaces were ground to ensure parallel alignment, with a misalignment error lower than 20 μm. In the case of the virgin material, two conventional strain gauges were glued to the lateral surfaces to obtain macro-strain curves. The front surface was ground down using P500, P1200, P2500 and P4000 grit paper (without water) and subsequently polished using 3 μm diamond paste and 0.04 μm colloidal silica suspension before etching the surface with Nital reagent for no longer than 5 s. This surface was sprayed with black paint to create the background before applying an airbrushed white speckle pattern. More details about the uniaxial experiment can be found in [16].

During the compression tests, two optical fibres illuminatee the sprayed surface while a digital camera (16-bit digitisation, 2048×2048 pixel array) recorded macroscopic images of the frontal surface (~20×20 mm^2) every 500 ms (see Fig. 4b). The pixel size was ~100 μm. YaDICs free software [24] was used to calculate the displacement fields.

(a)

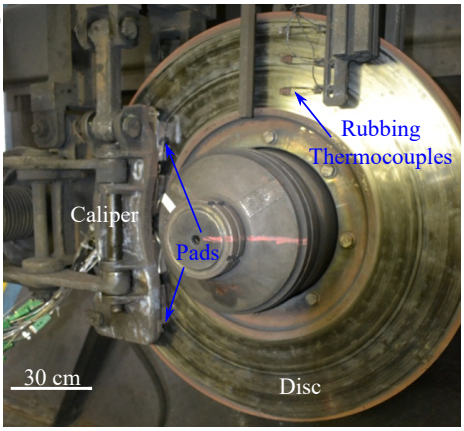

(b)

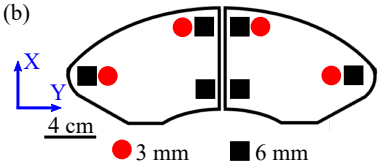

(c)

	N°	Initial speed (km/h)	Normal force (kN)	Simulated mass (t)	Braking duration (s)
Breaking-in	S1V0 x 5	80	5	5	18
Series 1	S1V1	80	5	5	22
	S1V2	120			33
	S1V3	160			44
	S1V4	200			55
	S1V5	250			69
Breaking-in	S2V0 x 5	80	36	5	18
Series 2	S2V1	80	36	7	20
	S2V2	120			31
	S2V3	160			41
	S2V4	200			51
	S2V5	250			65
Breaking-in	S3V0 x 5	80	45	5	18
Series 3	S3V1	80	45	9.5	20
	S3V2	120			31
	S3V3	160			41
	S3V4	200			51
	S3V5	250			65

Figure 3. (a) Image of the real-scale dynamometer set-up. (b) Localisation of the pad-inserted thermocouples located at 3 and 6 mm depth from the contact surface. (c) Table summarising the program carried out during the braking experiment.

This software uses the entire image as a sampling grid (*i.e.*, total sampling), and uses a bicubic interpolation for the grey level evaluation at non-integer coordinates. The Optical Flow elastic transform based on the Finite Element Model (OF-FEM) kinematics method is used with a discretized pixel subset of 14×14 pixels. The OF-FEM method reduces measurement uncertainties by ensuring the continuity of the found displacement field over the region of interest (ROI, see Fig 4b) [25]. The strain was computed from the displacement field using an in-house Python script. For the sake of simplicity, the study of the mechanical behaviour was limited to the normal strain (ε_{zz}). A good agreement was found between the DIC stress-strain curves and those obtained using gauges (although the DIC results tended to exhibit slightly lower strain values, >10%) and no significant out-of-plane effects were observed [22].

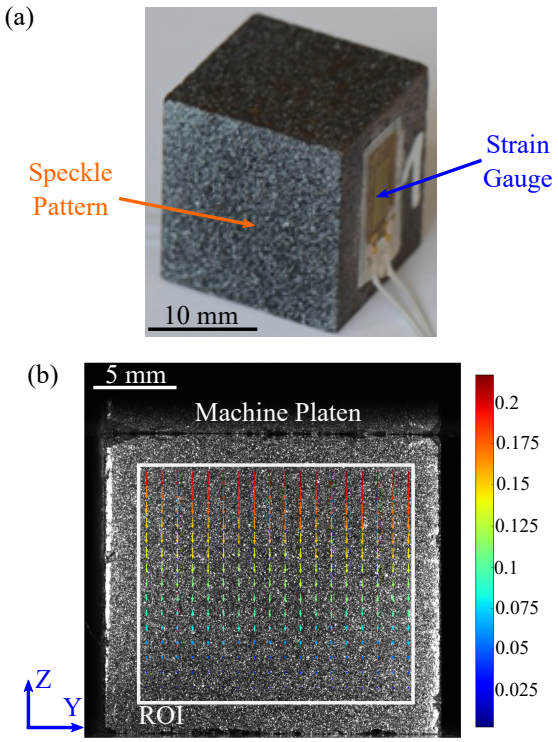

Figure 4. (a) Image of a 20×20×20 mm^3 cube, where a speckle pattern has been applied to the front surface and two strain gauges have been glued to the lateral surfaces. (b) Image of the experimental configuration of the compression test showing the ROI used for the computation of the vertical (Z) displacement field (expressed in units of pixel).

3. Results

3.1. Braking experiment

3.1.1. Thermal measurements

Fig. 5a shows the mean temperature obtained from the rubbing thermocouples (located on the disc and denoted in the figure by filled bars) and the 3 mm inserted thermocouples (located on the pad and denoted in the figure by empty bars). Some precautions must be taken when analysing these measurements. First, the disc-rubbing thermocouple results correspond to the mean of the measurements at the inner, medium and outer radius (see Fig. 3a). Apart from the fact that this provides an average value over the radius and the circumference, the main downside of these measurement is the fact is the contact continuity between the thermocouples and the disc is interrupted when the disc surface is not flat. This situation is observed during high-energy braking sequences, where thermo-mechanical effects usually lead to the formation of hotspots and undulating distortions [8]. Also, these perturbations are more significant with increasing speeds. Therefore, the values from the rubbing thermocouples have to be considered with caution, particularly in the case of high speed braking, where the thermocouples tend to measure values that are lower than the actual surface temperatures.

Wear of the brake pads induces a reduction in the distance between the contact surface and the inserted thermocouples. This effect becomes more intense with each subsequent braking series. Nevertheless, it is considered that, for similar heating levels, the reduction of thickness does not have a great impact on the temperature values because the thermal diffusivity of the sintered metallic matrix is known to be high. This point is confirmed by the small temperature difference (~100°C) observed between the recordings of 3 and 6 mm inserted thermocouples (Fig. 5b-c). Note that the wear reduction led to the destruction of one of the 3 mm inserted thermocouples (which occurred during S3V5, see bottom graph of Fig. 5b).

Fig. 5a shows that the pad temperature is close to that of the disc at low speeds, with increasing difference at higher speeds. These measured differences could be due to the contact interruptions between the rubbing thermocouples and

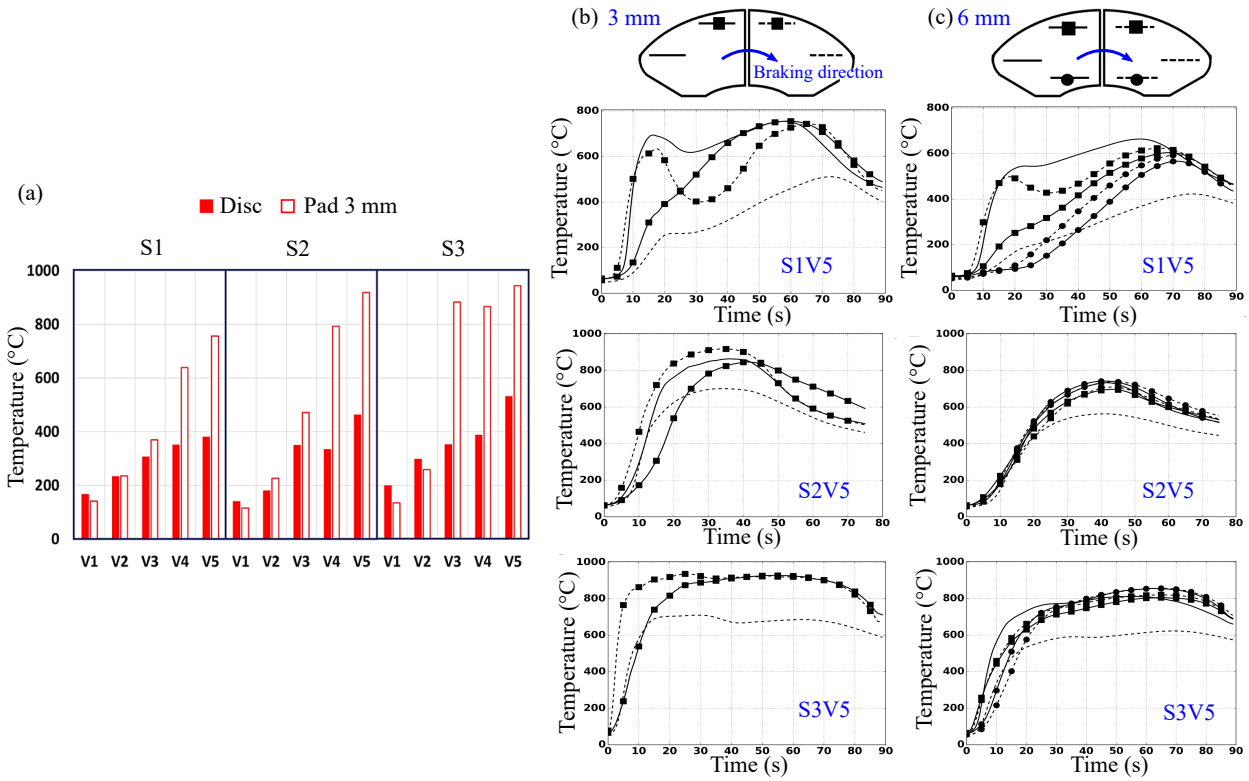

Figure 5. (a) Maximum temperatures in the disc (mean value of the rubbing thermocouple measurements) and pad (mean value of the measurements from the inserted thermocouples at 3 mm) for the three braking series. (b) 3 mm inserted thermocouples measurements for the three braking series at maximum speed (V5). (c) 6 mm inserted thermocouple measurements for the three braking series at maximum speed (V5). The legend for (b) and (c) is shown within the schematic brake-pad at the top of the graphs.

the disc, but also due to the fact that the disc temperature measurements are the mean of measurements at different radius lengths. The difference of measured temperature between the inner and outer radii is, thus, not accounted for and could be comparatively high. Nevertheless, a thermal gap between the disc and pad surfaces is often reported in braking applications. This is because the contact is permanent for the pad but not for the disc, which can be considered as an open thermodynamic system with alternating heating and cooling cycles. Therefore, higher temperatures are usually expected at the pad contact surface. Fig. 5a also shows increasing temperature levels, which correspond to increasing dissipated energies. Moreover, similar heating levels are observed between series of different speed and inertial mass when the dissipated energy and friction power have a similar magnitude (*e.g.,* S1V5, S2V4 and S3V3).

Fig. 5b shows the temperature recordings at maximum speed (V5) for the thermocouples located at 3 mm depth from the contact surface. The highest maximum temperature was reached during the S3 series (~1,000°C), which corresponds to the highest dissipated energy and friction power. The S3V5 results exhibit a plateau stage that can be related to saturation. Also, significant temperature variations are observed among the thermocouple locations for all series. These variations probably correspond to macroscopic discontinuities at the contact surface. It has been observed that the dynamic process of heating-dilatation-wear induced by friction leads to the loss of contact uniformity for brake-pad surfaces as extensive as the ones studied in this work [17, 26]. Similar contact alterations are observed in the case of 6 mm inserted thermocouples (Fig. 5c), although to a lower extend. Note that these levels of temperature, and corresponding thermomechanical stress, are able to induce material changes such as phase transformation or damage [18].

3.1.2. Friction

The instantaneous coefficient of friction (μa) and the mean friction coefficient (μm), noted as COF hereafter, was calculated following the UIC standard [27]. μa is calculated for any instant of braking by the ratio of the tangential

force (F_t) to the normal contact (F_b, $\mu a = F_t/F_b$). The tangential force is calculated by the ratio between the torque and the mean of the contact radius. The normal force is obtained from the pneumatic actuator pressure. The evolution of the COF during all braking sequences is shown in Fig. 6a. The fluctuations in friction during braking are higher in S1 as well as in the low speed sequences of S2 and S3 series. Such steep growths in the COF at low speed (*e.g.,* S1V1) are often observed when the evolution in friction mechanisms promotes adhesion effects [6]. The average COF in each braking sequence is shown in Fig. 6b, where two main tendencies can be observed. First, a stabilizing trend is observed over the series, with S3 exhibiting the lowest differences in COF. This stabilizing trend over the series indicates that the 3^{rd} body is evolving. Given the high level of thermal loading, it is likely that during S3 the tribological circuit is strongly activated, with various wear mechanisms occurring simultaneously (*i.e,* generation of wear sources from material damage and/or adhesion, debris accumulation as well as ruptures in the 3^{rd} body). Secondly, the friction level tends to be similar in for sequences with equivalent levels of energy dissipation (*e.g.,* S1V5, S2V4 and S3V3).

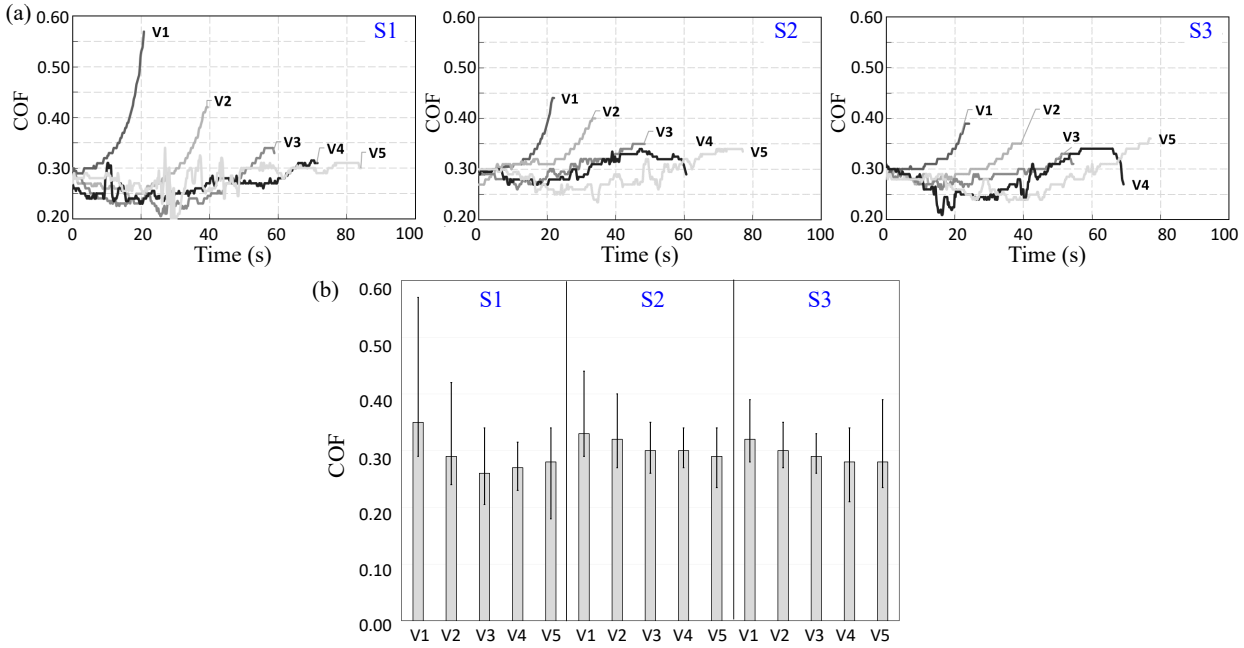

Figure 6. (a) Evolution of COF during braking for the three series. (b) COF average values (with error bars) for all braking series.

3.1.3. Surface analysis

Fig. 7a shows the contact surface for the right half-pad at the end of the braking program. This half-pad exhibits a macrocrack on the top-left region which seems to be caused by the presence of a 3 mm depth thermocouple. The main part of the contact surface seems to be covered by a thick layer of 3^{rd} body. In general, the examination of the contact surface indicates that the tribological circuit was fully developed when the program ended. The analysis at high magnification shows a compacted tribo-layer on the right of Fig. 7b, and some of the components (mostly graphites) lying on the left, where there is also a whole indicating the development of detachments. The red dashed square in Fig. 7a indicates the location from where the compression cube was carved out. Note that the disc exhibits a non-uniform deposit of 3^{rd} body material which spreads over the entire contact surface. Moreover, the infrared images confirm that the deposit heterogeneity is induced by the occurrence of hotspots.

3.2. Uniaxial loading-unloading tests

Fig. 8a shows the uniaxial compression protocol followed during the testing of the worn material. The virgin protocol is identical but with the pre-load is established at σ_{min} = 0.1 MPa instead of σ_{min} = 1 MPa. The tests start with a loading-unloading sequence at σ_{max} = 3 MPa, (five cycles are applied, $\Delta\sigma$ = 2 MPa) before complete release of the compression load. 2 to 3 minutes are necessary in-between loading/unloading cycles to change both the loading

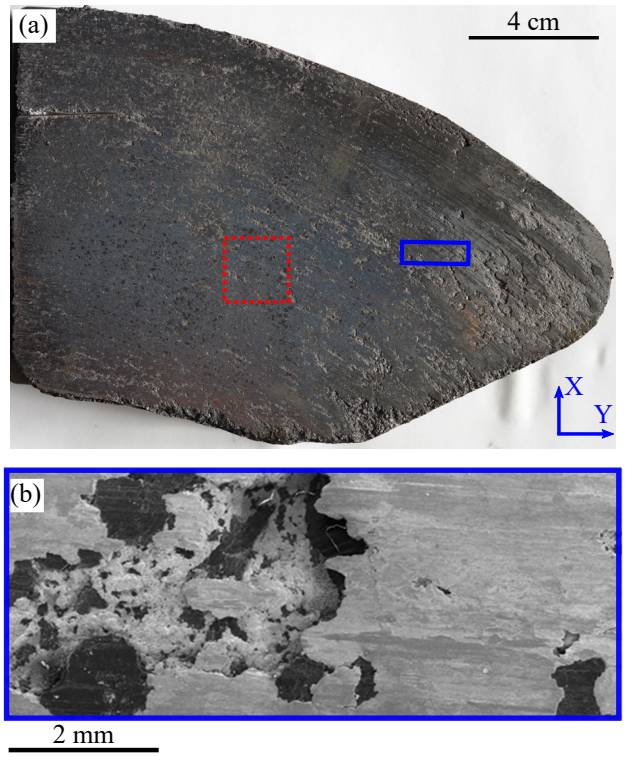

Figure 7. (a) Image of the contact surface of the right half-pad after the braking program. The red dashed square indicates the extraction location of the worn compression cube. (b) SEM (SE) image of the contact surface showing a compacted 3rd body and some graphite particles (in black).

and the image recording parameters. The maximum is subsequently increased to σ_{max} = 5 MPa, 10 MPa, 15 MPa, and 20 MPa. For the shake of simplicity, only the stress-strain curves at 20 MPa are shown in Fig. 8b (in this figure the strains are shown in negative values while stresses are kept positive).

Remarkably, the stress-strain curves shown in Fig. 8b have strong similarities with those reported in the literature for ceramics and rocks [28, 29]. Also, the yield point at which non-linear behaviour similar to plastic deformation first occurs was observed to first occur at 10 MPa in the virgin material. However, considerably micro-plasticity (due to the presence of graphite and ceramics inducing stress concentration in the metallic matrix) is expected to occur in the metallic matrix even at the lowest stress levels.

3.2.1. Virgin material

The virgin stress-strain curve (shown in blue in Fig. 8b) exhibits four main stages:

- At B1, the curve has an initial nearly perfect linear elasticity followed by yielding (B2 stage, with a $\Delta\varepsilon_{zz}$ = -0.27%) induced by the first loading at the 15-20 MPa stress level.
- B3 stage corresponds to the switching from loading to unloading and exhibits an apparent increase in stiffness.
- At the end of unloading (B4), the stiffness is 8% lower than in the forward B5 loading.
- The forward loading within the hysteresis loop (B5) is also nearly linear, with a slightly lower stiffness than that observed at B1.

Note that the loading/unloading cycles exhibit a strain *stays in hysteresis loop* behaviour ($\Delta\varepsilon_{zz}$ = -0.33%) and the residual strain at the minimum stress during B is $\varepsilon_{zz} \approx$ -0.2%.

The DIC ε_{zz} strain map (computed for a B5 loop-loading branch between 1 and 20 MPa, Fig. 8c) indicates a heterogeneous macroscopic deformation. The lowest strains ($\varepsilon_{zz} \approx$ -1.2%) are concentrated within and around Graphite 2

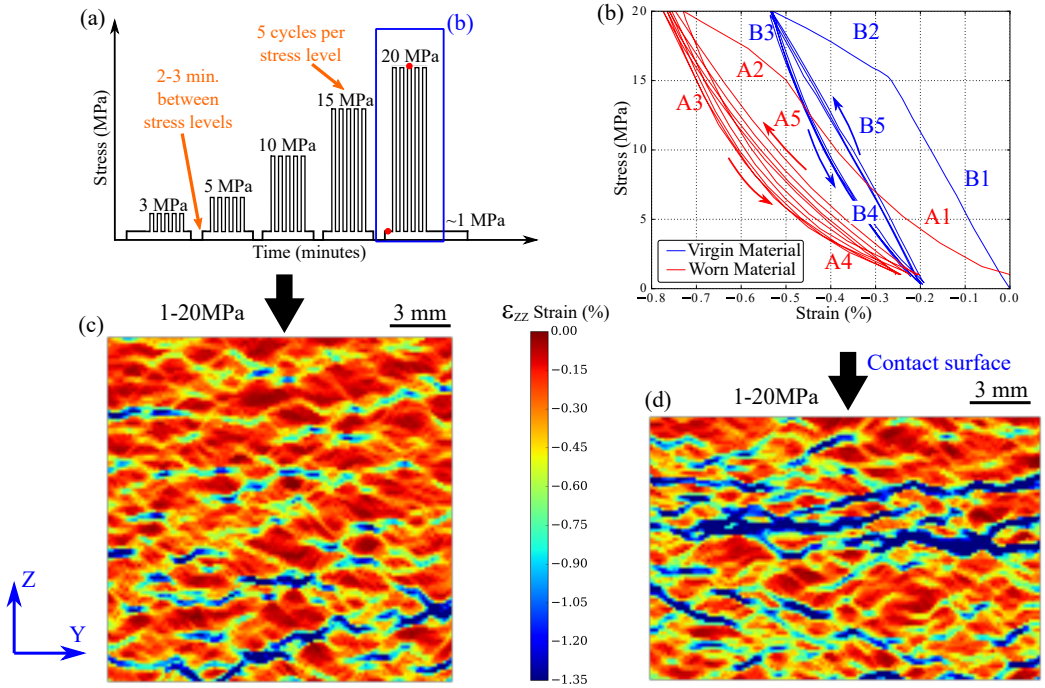

Figure 8. (a) Graph showing the different stages of the uniaxial loading/unloading protocol (compression loads are shown in positive values). (b) Stress-strain curves obtained from the DIC results for both virgin (in blue) and worn (in red) materials at 20 MPa stress level. (c) DIC map of the normal strain (ε_{zz}, expressed in %) for the virgin material. The map corresponds to a loading loop between 1 and 20 MPa (indicated by two red dots in (a)). (d) DIC map of the normal strain (ε_{zz}, expressed in %) for the worn material. The top of the map corresponds to the contact surface.

particles [30], leading to the formation of deformation bands. In this case the bands are more pronounced at the bottom of the sample, but the examination of other samples of the same material indicates a random location of the bands depending on the positioning of Graphite 2 particles. The formation of deformation bands has been reported in the literature for a cellular Al alloy [31] as well as for a low-density porous copper material [32]. In addition, the effect of strain localisation induced by the presence of graphite particles has been observed in cast iron materials [33, 34], although in this case the strain localisation occurs at the microscopic scale length.

3.3. Worn material

The worn stress-strain curve (shown in red in Fig. 8b) exhibits five main stages with three main differences compared to the virgin material:

- At A1, the curve has an initial **settling down** phase followed by a nearly linear region at higher load levels.
- Yielding is also observed to occur during the *first* loading at the 15-20 MPa stress level (A2 stage, with a $\Delta\varepsilon_{zz}$ = -0.23%). Note that, during an actual braking situation, the mean normal load is not expected to reach these high values (15-20 MPa), although it is likely that these values could occur locally due to the material heterogeneity.
- A3 stage corresponds to the switching from loading to unloading and also exhibits a relatively increased stiffness.
- At the end of the unloading (A4), the **stiffness is similar** to the *settling down* phase of the forward loading A1.
- The forward loading within the hysteresis loop (A5) is **non-linear**.

In this case, the general stiffness is lower and therefore higher values of strain are induced ($\Delta\varepsilon_{zz} \approx$ -0.53% is observed within the loading/unloading cycles). Moreover, the area within the hysteresis loop is smaller than in the

virgin material and the loading/unloading branches do not follow the exact same paths between cycles; in other words, the strain *stays in hysteresis loop* behaviour is less noticeable in the worn material. The amount of yielding and residual strains ($\Delta\varepsilon_{zz} \approx$ -0.25% and $\Delta\varepsilon_{zz} \approx$ -0.2%, respectively) seems to be similar for both materials. Note that the occurrence of the non-linear settling down phase (observed in A1 and A5) is usually related to the presence of damage. In the case of cracking media such as brittle rock, this phenomenon is linked to the closure of microcracks [35].

The DIC ε_{zz} strain map of the worn material (Fig. 8d) also indicates a heterogeneous macroscopic deformation with a marked strain band occurring at ~4 mm from the contact surface. In this case, the presence of such large deformation bands cannot be exclusively correlated to the presence of Graphite 2 particles. On the contrary, the bottom region of this sample exhibits strain localisation occurring at/around Graphite 2 particles, similar to the one observed in the virgin material.

Highly strained deformation band (HSDB). The effects on the mechanical response induced by the presence of this band has been studied in detail by comparing the DIC ε_{zz} strain maps computed for loop-unloading branches at different stress levels (Fig. 9). An additional DIC computation is performed between the stages noted as *10 min* and *2 s* after the sample is fully unloaded (Fig. 9a). At 3-1 MPa (Fig. 9b), the mean strain unloading values are close to 0.1%, although a small band showing 0.35% values is observed on the right middle of the image. At 5-1 MPa (Fig. 9c), the strain localisation only takes place within the region identified as HSDB. The highest strain values observed in this region are close to 1.0 %. At 10-1 MPa, 15-1 MPa and 20-1 MPa (Fig. 9d-f), the strain localisation is progressively extended to the bottom region of the sample. Interestingly, a time-dependent unloading effect is observed in Fig. 9g, mainly occurring within the HSDB region. The strain values occurring in this region are close to 0.1%, and the mean ε_{zz} calculated from the image yields a negligible unloading of 0.016%. Finally, note that the regions exhibiting the highest strain levels (for instance, red in Fig. 9f) during the loop-unloading correspond to the regions with the lowest strain levels during the loop-loading (blue in Fig. 8d). These results indicate that the compression behaviour of the worn material is mainly controlled by the HSDB region where the strain localisation is maximal.

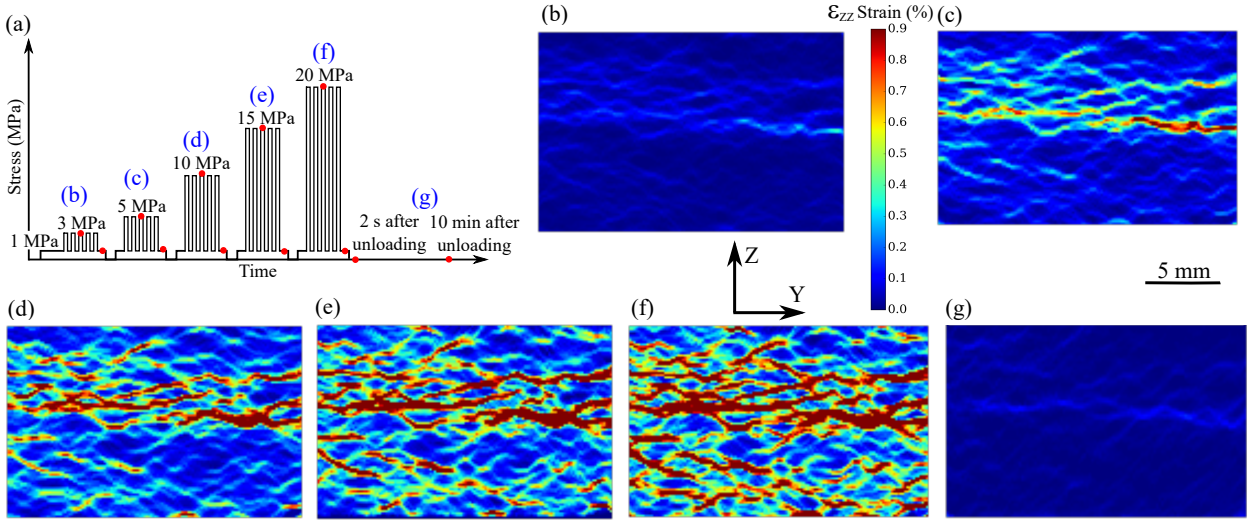

Figure 9. (a) Graph showing the different stages of the uniaxial loading/unloading protocol. The red dots indicate the images used for the computation of ε_{zz} strain maps: (b) at 3-1 MPa, (c) 5-1 MPa, (d) 10-1 MPa, (e) 15-1 MPa, (f) 20-1 MPa, and (g) between an image taken 10 min after sample unloading and one taken immediately after sample unloading.

Layered bulk behaviour. The use of layered ROIs (Fig. 10a) allows the study of the local mechanical behaviour at three different depths (noted as top, middle and bottom). The stress-strain curves obtained from the local DIC computations are shown in Fig. 10b. The top layer behaviour shows an initial and relatively small *settling down* phase followed by a nearly linear region at higher load levels. No plastic deformation and very small residual strain ($\Delta\varepsilon_{zz} \approx$ -0.05%) are observed. The hysteresis can be considered as non-existent. The behaviour of the middle layer is very similar to the worn curve shown in Fig. 8b but with higher strains observed within the loading/unloading cycles

($\Delta\varepsilon_{zz} \approx$ -0.8% against $\Delta\varepsilon_{zz} \approx$ -0.42%). The hysteresis seems to be slightly increased. This result additionally confirm the above conclusion about the HSDB region controlling the macroscopic mechanical behaviour of the worn material. By contrast, the behaviour of the bottom layer is quasi-linear and exhibits lower stiffness when compared to the virgin material. This reduction in the stiffness could be explained by the development of microcracks. Further, the bottom *stays in hysteresis loop* behaviour is less noticeable when compared to that of the virgin material.

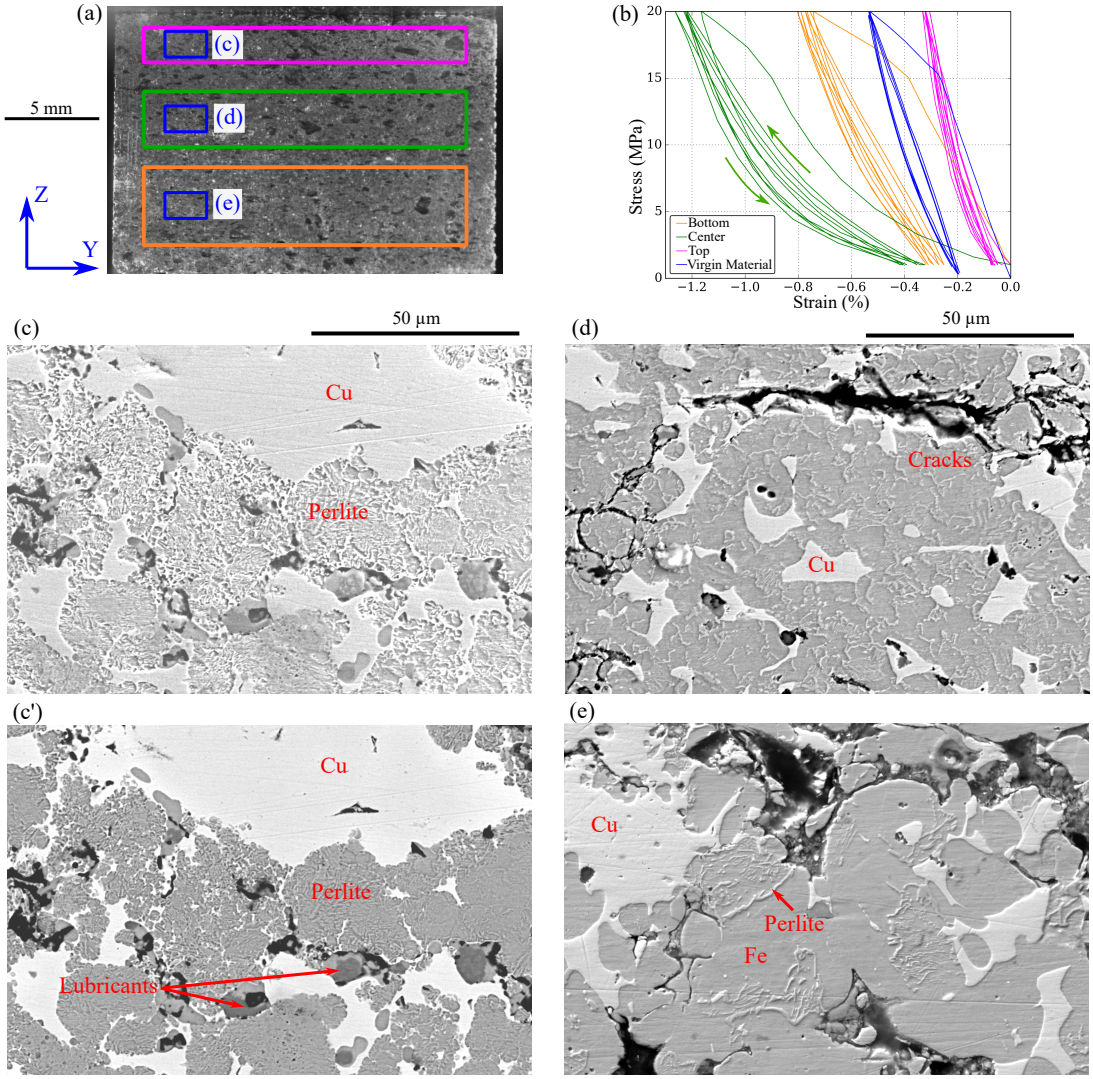

Figure 10. (a) Light-optical image of the worn sample showing the ROI locations used in the DIC computations of the top, middle and bottom layers. (b) Stress-strain curves of the top, middle and bottom layers at 20 MPa stress level. The virgin curve is added in blue for comparison purposes. (c) SE image and (c') BSE image of the microstructure within the top layer. (d) SE image of the microstructure within the middle Layer. (e) SE image of the microstructure within the bottom layer. See Fig. 1c-d for comparison with the virgin material.

Microstructural changes. The analysis of the microstructure indicates a carburization-like effect occurring in the Fe-phase. In the top layer, the Fe-phase is completely covered by pearlite (Fig. 10c-c'). In the middle layer, the colonies of pearlite are homogeneously distributed throughout the Fe-phase (Fig. 10d). The microstructure in the bottom (Fig. 10e) layer is similar that observed in the virgin material (Fig. 1c-d).

Microcracking. The visual evaluation of the SEM images does not allow a thorough investigation of the microcrack density. Nevertheless, it is sufficient to determine an increased content of microcracks within the middle layer

(Fig. 11). No macrocrack is observed, although the possibility of a bulk 3D linkage between microcraks must be considered. The content of microcracks within the top and bottom layers seems similar, although this statement is conjectural. Note that the virgin material also exhibits some microcracking after the uniaxial compression test. The orientation of cracks seems random, as horizontal, oblique and vertical cracks can be indistinctly observed. These microcracks tend to occur at the thin walls of metallic matrix laying between large Graphite 2 particles. Finally, some out-of-plane features can be observed in (Fig. 11). These out-of-plane features are also observed within the top and bottom layers although they are less noticeable.

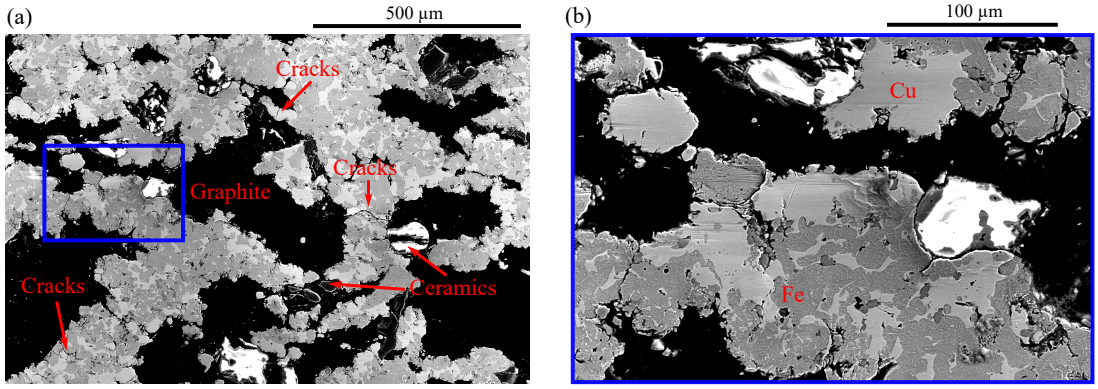

Figure 11. (a) SE image of the mesostructure within the middle layer. Charging effects are observed on some ceramic particles. (b) Detail of the microcracks. See Fig. 1b for comparison with the virgin material.

Hardness. Vickers hardness tests were performed using an instrumented indentation machine (with about 10 points per layer and up to 120 N of multi-cycling). The reported values correspond to the Martens hardness, computed from the maximum displacement of the load-displacement curves (see Table 2). The highest values (+30%) are observed in the top layer. The hardness of middle and bottom layers is similar to that of the virgin material. These results are in good agreement with the increased content of carbon observed in the Fe-phase of the top layer. The high dispersion of these measurements is related to the material heterogeneity, which gives a different response depending on which phase/particles are being indented, as well as on the arrangement of these phases/particles within the volume.

Virgin Material	**Worn Material**		
	Top	**Middle**	**Bottom**
0.30(0.21)	0.46(0.31)	0.31(0.18)	0.32(0.20)

Table 2. Martens hardness in GPa (standard deviation) of the virgin and worn materials. The worn material is subdivided into the three regions identified in Fig. 10a.

4. Discussion

4.1. Evolution of the compression behaviour related to the microstructure

Fig. 12 summarizes the main findings concerning the evolution of the compression behaviour and microstructure. The virgin material exhibits a complex mechanical behaviour where Graphite 2 particles, which are softer than the matrix, induce strain localisation in the form of macroscopic deformation bands (Fig. 12a, shown in green and blue). After the compression, some microcracking can be distinguish on the SEM images (Fig. 12c). Additional compression tests, not shown here for the sake of simplicity, indicate that the Graphites 2 particles control the formation of hysteresis (the graphite material is known for having intrinsic hysteretic behaviour [36]). Nonetheless, there are other factors (*e.g.,* energy dissipation induced by friction between Graphite 2 particles and the metallic matrix walls) that might also contribute, in some extent, to the hysteresis loop.

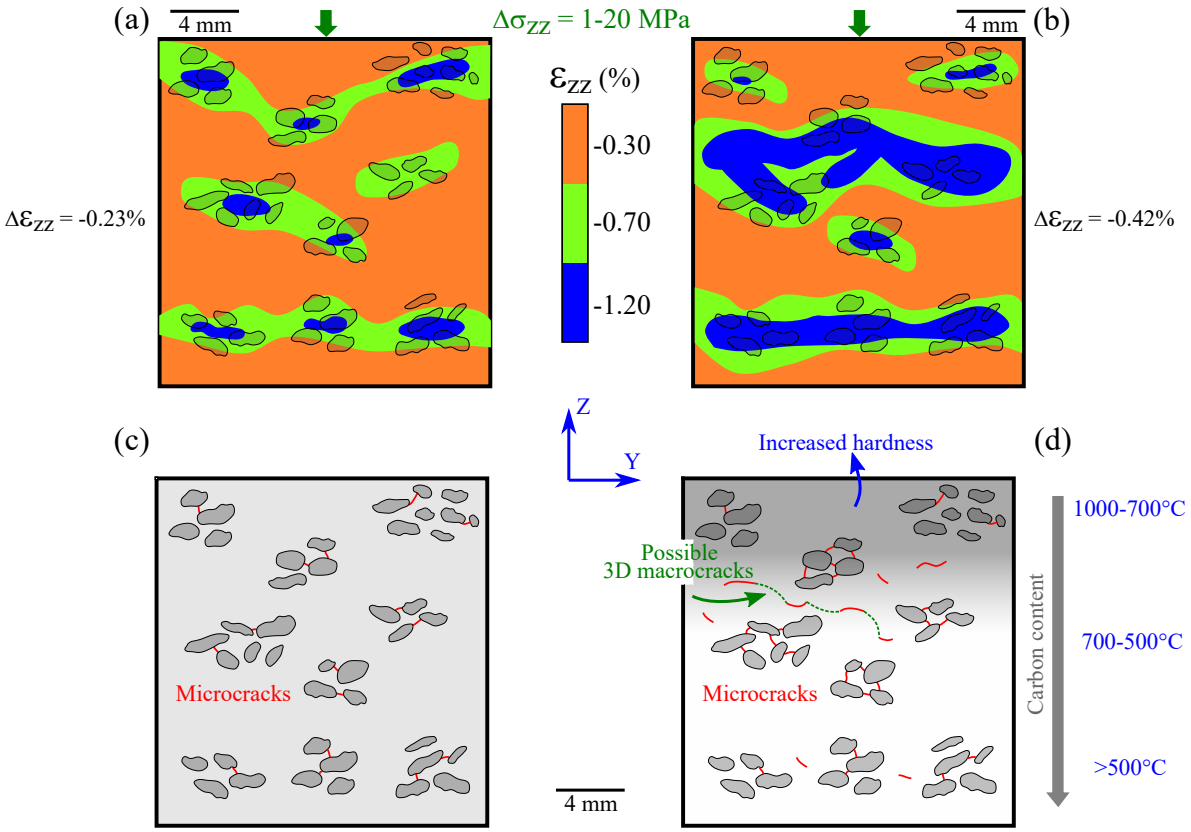

Figure 12. (a) Schematic illustration of the strain localisation occurring in the virgin material (b) and the worn material when tested in a loop-loading branch between 1 and 20 MPa. (c) Schematic illustration of the microcracking observed in the virgin material at the end of the compression test. (d) Schematic illustration of the microcracking and level of carbon diffusion observed in the worn material at the end of the compression test. The arrow indicates that the carbon content in the Fe-phase decreases along the depth. The temperature gradient is an estimation based on the thermocouple results.

The mechanical response of the worn material is even more complex than that of the virgin one. The changes induced by the braking program led to the formation of a tri-layered-like material. Strain localisation is also observed, but there are variations depending on the layer (Fig. 12b). The carbon diffusion is more important in the top layer (Fig. 12d, temperatures as high as 800-1000°C). This is consistent with the fact that the austenitization occurring at 800-1000°C enhances carbon diffusion (the solubility of C is greater in austenite compared to ferrite [37]). Thus, we consider that the mechanical changes observed in the top layer (increased Young's modulus and hardness) are mainly induced by carbon diffusion. Furthermore, the lack of yielding observed in the top layer (Fig. 10b) would be due to a carbon-induced increase in the elastic limit (σ_y) of the Fe-phase.

As is the case in geological materials, the pronounced non-linearity (Fig. 10b) exhibited by the middle layer is probably related to the high content of microcracks. Moreover, it has been reported [29] that an increased microcrack content leads to the increase of the area enclosed within the hysteresis loop. Also, the reduced reversibility in the hysteresis loop of the middle layer (*i.e.,* the *stays in hysteresis loop* behaviour is less noticeable) could be linked to enhanced crack closure effects such as higher friction between the crack lips. On the other hand, it is probable that the time-dependent recovery observed in Fig. 9g is controlled by the intrinsic hysteretic behaviour of Graphite 2 particles rather than by crack closure effects. Even if we were not able to confirm this point, the possibility of 3D macrocracks resulting from the coalescence of microcracks should be contemplated (Fig. 12d). Note that the compression curve of the bottom layer (Fig. 10b) also suggests an increased microcrack density when compared to the virgin material.

The combination of mechanical loading (shear and compression) with constrained thermal expansions and microstructural transformations could explain the higher microcrack density observed in the middle layer. Neverthe-

less, the Fe-phase microstructural transformation (*i.e.,* higher content of C within the lattice structure combined with austenitization cycles) seems to be the key parameter controlling the increase in microcrack density. This is because the depth of the middle layer mainly corresponds to the range of temperature (800-700°C) where the Fe-phase transitions from ferrite to austenite (Fig. 12d). This transition would induce a boundary effect, which promotes the localisation of stresses. In any case, the elucidation of the mechanisms leading to the increase of microcracks observed in the middle layer needs further research mostly concerning material science (*e.g.,* the use of diffraction techniques for phase analysis).

Finally, given that the virgin material is considerably porous (see Section 2.1) and its tendency to microcrack, the residual stresses induced by Fe-phase transformation as well as the different dilatation coefficient of components are considered to play a minor role in the evolution of the compressive behaviour.

4.2. Evolution of the friction behaviour related to the contact surface and sub-surface material

At low temperature (S1V1-S1V3, S2V1-S2V2, S3V1-S3V2, see Fig. 6b) the COF values are higher and more variable when compared to those occurring at high temperature (S1V4-S1V5, S2V3-S2V5, S3V3-S3V5). These results correlate well with the fact that the friction tends to be more abrasive at low temperature and more adhesive at high temperature [38]. They also provide a demonstration of the role that temperature level plays in COF stabilization. For instance, a significant stabilization can be observed during the S1V4 braking sequence. During this sequence, a temperature higher than 700°C is reached for the first time at the contact surface (more than 600°C is registered by thermocouples at 3 mm, Fig. 6b). As discussed in Section 4.1, ferrite to austenite transformation starts at temperatures above ~700°C. At this temperature, the copper is able to endure higher levels of plastic yielding. It is generally accepted that the increase of copper ductility contributes to the development of a tribolayer that facilitates the stabilization of the COF [39]. Thus, opposing mechanisms develop during the braking program: the hardness of the sub-surface material increases due to carbon diffusion while the copper contributes to an increase in the ductility of the tribolayer. The effect that an increasing sub-surface hardness has on the ductility of the tribolayer has yet to be determined. However, an increase in the brake-pad hardness usually leads to an increase in the wear rates of the counter-face (*i.e.,* the disc). This aspect could not be investigated in the present study because it would require long-term tests, but the results of endurance tests conducted by the industrial partner confirms this trend.

4.3. Limitations and open questions

The combination of thermal monitoring and bulk properties characterization has led to an in-depth understanding of the mechanisms involved in the evolution of the compression behaviour. Nevertheless, so far we can only conjecture about the influence of the material evolution on the braking performance. Some of the most relevant issues concern:

Contact uniformity. The results shown in Fig. 5 indicate the development of different thermal gradients depending on the pad location. A spatially heterogeneous mechanical behaviour can be therefore expected over the contact surface. The spatial variation of the mechanical properties usually leads to a reduced contact uniformity and subsequent thermal localisations. In this work, however, the mechanical heterogeneity could be neutralized by the reduced stiffness of the middle layer.

Durability. The damage localisation observed in the middle layer can be considered as highly detrimental to the brake-pad durability. It would be interesting to investigate whether this damage could eventually lead to the final failure of the brake-pad.

Vibrations. A reduction in vibrations could be expected given the decrease in stiffness (Fig 8b) and the dominant role of Graphite 2 particles in the middle layer (Fig 9). However, a decreasing effect resulting from the increase in stiffness and hardness of the top layer should be considered.

Tribology. The spatial heterogeneity of the thermal loading most likely affects the 3^{rd} body composition. As is the case for contact uniformity, one could argue that a spatially heterogeneous 3^{rd} body can hamper the stabilization of COF and even increase wear rates by lowering the cohesiveness of the layer.

Ideally, the evolution of material properties should contribute to the further stabilization of the COF and 3^{rd} body. Further investigation on the subject requires the design of highly instrumented dynamometers accounting for the monitoring of other parameters (*e.g.,* vibrations), the implementation of multi-loading tests (*e.g.,* to investigate the effect of shear load), as well as a detailed characterization of the 3^{rd} body composition (*e.g.,* the use of Focused Ion Beam (FIB-SEM) to map the chemical composition and microstructure over the contact surface).

5. Conclusions

The changes in bulk properties induced by a braking program were investigated using a *simplified* semi-metallic friction material. The use of inserted thermocouples enabled the monitoring of the thermal loading while the characterization of the compressive and microstructural properties was carried out using compression tests coupled with DIC and SEM analysis. The following conclusions can be drawn:

1. The thermal loading plays a dominant role in the evolution of the friction behaviour and material properties.
2. The stiffness of the worn material is lower and the evolution in the material properties leads to a compression behaviour similar to that of a tri-layered material.
3. The changes in the worn material compression behaviour are related to the microstructure:
   (a) The increased microcrack density of the central portion of the brake-pad thickness leads to the formation of a deformation band containing, in turn, the maximum (during unloading) or minimum (during loading) strain values.
   (b) An increase in the carbon content (in the form of perlite colonies) is observed in the Fe-phase. The increase in carbon content is particularly important in the top layer, which exhibits the highest stiffness and hardness.
4. The results indicate that the material evolution has deleterious effects on the contact quality (spatial variation of the mechanical behaviour over the brake-pad cross section), durability (localisation of damage favouring material fragmentation) and tribology (spatial variation of the 3^{rd} body composition).

Even if the tribological aspects are to be prioritised, the bulk behaviour should also be considered when developing new formulations. Understanding the interactions between components at the microstructural level gives valuable insight into possible ways to improve the material formulation. For example, the results presented here indicate that the carbon diffusion has negative effects. Thus, new formulations ensuring reduction in carbon diffusion can be envisaged. Hence, the further investigation of the evolution of friction material properties with special emphasis on the quantification of the subsequent effects on the braking performance is recommended.

Acknowledgments

The present investigation was supported by the International Campus on Safety and Inter-modality in Transportation, the Hauts-de-France's the Regional Delegation for Research and Technology, the European Union, the Ministry of Higher Education and Research, the French National Research Agency (ANR COMATCO), the ELSAT project, and the National Center for Scientific Research (CNRS). The authors gratefully acknowledge these institutions for their support. FLERTEX SINTER Company is acknowledged for supplying the studied material and lending the dynamometer where the experiments were performed. Special gratitude is expressed to Tyler Oesch for his thoughtful advice and guidance.

References

[1] P. J. Blau, Compositions, functions, and testing of friction brake materials and their additives, Tech. rep., Oak Ridge National Lab., TN (US) (2001).
URL http://www.osti.gov/scitech/biblio/788356

[2] W. Österle, A. Dmitriev, Functionality of conventional brake friction materials – Perceptions from findings observed at different length scales, Wear 271 (9-10) (2011) 2198 – 2207, 18th International Conference on Wear of Materials. doi:http://dx.doi.org/10.1016/j.wear.2010.11.035.
URL http://www.sciencedirect.com/science/article/pii/S0043164811001591

[3] M. Eriksson, F. Bergman, S. Jacobson, On the nature of tribological contact in automotive brakes, Wear 252 (1) (2002) 26 – 36. doi:https://doi.org/10.1016/S0043-1648(01)00849-3.
URL http://www.sciencedirect.com/science/article/pii/S0043164801008493

[4] W. Österle, M. Griepentrog, T. Gross, I. Urban, Chemical and microstructural changes induced by friction and wear of brakes, Wear 251 (1) (2001) 1469 – 1476, 13th International Conference on Wear of Materials. doi:https://doi.org/10.1016/S0043-1648(01)00785-2.
URL http://www.sciencedirect.com/science/article/pii/S0043164801007852

[5] A.-L. Cristol-Bulthé, Y. Desplanques, G. Degallaix, Y. Berthier, Mechanical and chemical investigation of the temperature influence on the tribological mechanisms occurring in omc/cast iron friction contact, Wear 264 (9) (2008) 815 – 825, papers presented at the 12th Nordic Symposium on Tribology, NORDTRIB 2006. doi:https://doi.org/10.1016/j.wear.2006.12.080.
URL http://www.sciencedirect.com/science/article/pii/S0043164807005534

[6] Y. Desplanques, O. Roussette, G. Degallaix, R. Copin, Y. Berthier, Analysis of tribological behaviour of pad–disc contact in railway braking: Part 1. laboratory test development, compromises between actual and simulated tribological triplets, Wear 262 (5) (2007) 582 – 591. doi:https://doi.org/10.1016/j.wear.2006.07.004.
URL http://www.sciencedirect.com/science/article/pii/S0043164806002936

[7] Y. Xiao, Z. Zhang, P. Yao, K. Fan, H. Zhou, T. Gong, L. Zhao, M. Deng, Mechanical and tribological behaviors of copper metal matrix composites for brake pads used in high-speed trains, Tribol. Int. 119 (2018) 585 – 592. doi:https://doi.org/10.1016/j.triboint.2017.11.038.
URL http://www.sciencedirect.com/science/article/pii/S0301679X17305522

[8] S. Panier, P. Dufrénoy, D. Weichert, An experimental investigation of hot spots in railway disc brakes, Wear 256 (7) (2004) 764 – 773. doi:https://doi.org/10.1016/S0043-1648(03)00459-9.
URL http://www.sciencedirect.com/science/article/pii/S0043164803004599

[9] M. Kumar, X. Boidin, Y. Desplanques, J. Bijwe, Influence of various metallic fillers in friction materials on hot-spot appearance during stop braking, Wear 270 (5) (2011) 371 – 381. doi:https://doi.org/10.1016/j.wear.2010.11.009.
URL http://www.sciencedirect.com/science/article/pii/S0043164810004230

[10] T. J. Mackin, S. C. Noe, K. Ball, B. Bedell, D. Bim-Merle, M. Bingaman, D. Bomleny, G. Chemlir, D. Clayton, H. Evans, R. Gau, J. Hart, J. Karney, B. Kiple, R. Kaluga, P. Kung, A. Law, D. Lim, R. Merema, B. Miller, T. Miller, T. Nielson, T. O'Shea, M. Olson, H. Padilla, B. Penner, C. Penny, R. Peterson, V. Polidoro, A. Raghu, B. Resor, B. Robinson, D. Schambach, B. Snyder, E. Tom, R. Tschantz, B. Walker, K. Wasielewski, T. Webb, S. Wise, R. Yang, R. Zimmerman, Thermal cracking in disc brakes, Eng. Fail. Anal. 9 (1) (2002) 63 – 76. doi:https://doi.org/10.1016/S1350-6307(00)00037-6.
URL http://www.sciencedirect.com/science/article/pii/S1350630700000376

[11] F. Bagnoli, F. Dolce, M. Bernabei, Thermal fatigue cracks of fire fighting vehicles gray iron brake discs, Eng. Fail. Anal. 16 (1) (2009) 152 – 163. doi:https://doi.org/10.1016/j.engfailanal.2008.01.009.
URL http://www.sciencedirect.com/science/article/pii/S1350630708000241

[12] M. Boniardi, F. D'Errico, C. Tagliabue, G. Gotti, G. Perricone, Failure analysis of a motorcycle brake disc, Eng. Fail. Anal. 13 (6) (2006) 933 – 945. doi:https://doi.org/10.1016/j.engfailanal.2005.04.012.
URL http://www.sciencedirect.com/science/article/pii/S1350630705001500

[13] Z. Yang, J. Han, W. Li, Z. Li, L. Pan, X. Shi, Analyzing the mechanisms of fatigue crack initiation and propagation in CRH EMU brake discs, Eng. Fail. Anal. 34 (2013) 121 – 128. doi:https://doi.org/10.1016/j.engfailanal.2013.07.004.
URL http://www.sciencedirect.com/science/article/pii/S135063071300232X

[14] H. Kasem, J. Brunel, P. Dufrénoy, M. Siroux, B. Desmet, Thermal levels and subsurface damage induced by the occurrence of hot spots during high-energy braking, Wear 270 (5) (2011) 355 – 364. doi:https://doi.org/10.1016/j.wear.2010.11.007.
URL http://www.sciencedirect.com/science/article/pii/S0043164810004217

[15] Z. Li, J. Han, Z. Yang, W. Li, Analyzing the mechanisms of thermal fatigue and phase change of steel used in brake discs, Eng. Fail. Anal. 57 (2015) 202 – 218. doi:https://doi.org/10.1016/j.engfailanal.2015.07.002.
URL http://www.sciencedirect.com/science/article/pii/S1350630715300017

[16] R. Mann, V. Magnier, J.-F. Brunel, F. Brunel, P. Dufrénoy, M. Henrion, Relation between mechanical behavior and microstructure of a sintered material for braking application, Wear 386-387 (2017) 1 – 16. doi:https://doi.org/10.1016/j.wear.2017.05.013.
URL http://www.sciencedirect.com/science/article/pii/S0043164817300923

[17] P. Dufrénoy, Two-/three-dimensional hybrid model of the thermomechanical behaviour of disc brakes, Proceedings of the Institution of Mechanical Engineers, Part F: Journal of Rail and Rapid Transit 218 (1) (2004) 17–30. arXiv:https://doi.org/10.1243/095440904322804402, doi:10.1243/095440904322804402.
URL https://doi.org/10.1243/095440904322804402

[18] K. Lee, J. R. Barber, Frictionally Excited Thermoelastic Instability in Automotive Disk Brakes, J. Tribol. 115 (4) (1993) 607–614. doi:10.1115/1.2921683.
URL http://dx.doi.org/10.1115/1.2921683

[19] M. Graf, G.-P. Ostermeyer, Efficient computation of thermoelastic instabilities in the presence of wear, Wear 312 (1) (2014) 11 – 20. doi:

https://doi.org/10.1016/j.wear.2014.01.008.
URL http://www.sciencedirect.com/science/article/pii/S0043164814000258
[20] A. Heussaff, L. Dubar, T. Tison, M. Watremez, R. Nunes, A methodology for the modelling of the variability of brake lining surfaces, Wear 289 (2012) 145 – 159. doi:https://doi.org/10.1016/j.wear.2012.04.002.
URL http://www.sciencedirect.com/science/article/pii/S0043164812000981
[21] V. Magnier, D. N. Ramasami, J. Brunel, P. Dufrénoy, T. Chancelier, History effect on squeal with a mesoscopic approach to friction materials, Tribol. Int. 115 (2017) 600 – 607. doi:https://doi.org/10.1016/j.triboint.2017.06.031.
URL http://www.sciencedirect.com/science/article/pii/S0301679X17303195
[22] M. Sutton, J. Yan, V. Tiwari, H. Schreier, J. Orteu, The effect of out-of-plane motion on 2D and 3D digital image correlation measurements, Opt. Lasers Eng. 46 (10) (2008) 746 – 757. doi:https://doi.org/10.1016/j.optlaseng.2008.05.005.
URL http://www.sciencedirect.com/science/article/pii/S0143816608000985
[23] D. Paganin, S. C. Mayo, T. E. Gureyev, P. R. Miller, S. W. Wilkins, Simultaneous phase and amplitude extraction from a single defocused image of a homogeneous object, J. Microsc. 206 (1) (2002) 33–40. arXiv:https://onlinelibrary.wiley.com/doi/pdf/10.1046/j.1365-2818.2002.01010.x, doi:10.1046/j.1365-2818.2002.01010.x.
URL https://onlinelibrary.wiley.com/doi/abs/10.1046/j.1365-2818.2002.01010.x
[24] U. Lille:, Yadics software.
URL http://yadics.univ-lille1.fr/wordpress/
[25] F. Hild, S. Roux, Digital image correlation. Optical methods for solid mechanics: a full-field approach, Wiley-VCH, Berlin (Germany), 2012.
URL http://www.wiley-vch.de/de/fachgebiete/ingenieurwesen/optical-methods-for-solid-mechanics-978-3-527-41111-5
[26] R. Mann, Experiments and thermomechanical modelling of braking application & friction material characterization with loading history effect, Ph.D. thesis, University of Lille (2017).
[27] Frein - frein à disques et leur utilisation - conditions générales pour la certification de garnitures de frein.
URL https://uic.org/IMG/pdf/f541x3_anl_i_07-18.pdf
[28] G. Bruno, M. Kachanov, Microstructure–property connections for porous ceramics: The possibilities offered by micromechanics, J. Am. Ceram. Soc. 99 (12) (2016) 3829–3852. arXiv:https://onlinelibrary.wiley.com/doi/pdf/10.1111/jace.14624, doi:10.1111/jace.14624.
URL https://onlinelibrary.wiley.com/doi/abs/10.1111/jace.14624
[29] E. David, N. Brantut, A. Schubnel, R. Zimmerman, Sliding crack model for nonlinearity and hysteresis in the uniaxial stress–strain curve of rock, Int. J. Rock Mech. Min. Sci. 52 (2012) 9 – 17. doi:https://doi.org/10.1016/j.ijrmms.2012.02.001.
URL http://www.sciencedirect.com/science/article/pii/S1365160912000317
[30] Mann, Ruddy, Magnier, Vincent, Serrano-Munoz, Itziar, Brunel, Jean-Francois, Brunel, Florent, Dufrenoy, Philippe, Henrion, Michele, Non-linear mechanical behavior of a sintered material for braking application using digital image correlation, Mechanics & Industry 18 (6) (2017) 601. doi:10.1051/meca/2017031.
URL https://doi.org/10.1051/meca/2017031
[31] H. Bart-Smith, A.-F. Bastawros, D. Mumm, A. Evans, D. Sypeck, H. Wadley, Compressive deformation and yielding mechanisms in cellular Al alloys determined using X-ray tomography and surface strain mapping, Acta Mater. 46 (10) (1998) 3583 – 3592. doi:https://doi.org/10.1016/S1359-6454(98)00025-1.
URL http://www.sciencedirect.com/science/article/pii/S1359645498000251
[32] M. Hakamada, Y. Asao, T. Kuromura, Y. Chen, H. Kusuda, M. Mabuchi, Density dependence of the compressive properties of porous copper over a wide density range, Acta Mater. 55 (7) (2007) 2291 – 2299. doi:https://doi.org/10.1016/j.actamat.2006.11.024.
URL http://www.sciencedirect.com/science/article/pii/S1359645406008354
[33] T. Sjögren, P. E. Persson, P. Vomacka, Analysing the deformation behaviour of compacted graphite cast irons using digital image correlation techniques, in: Science and Processing of Cast Iron IX, Vol. 457 of Key Engineering Materials, Trans Tech Publications, 2011, pp. 470–475. doi:10.4028/www.scientific.net/KEM.457.470.
[34] J. Pina, S. Shafqat, V. Kouznetsova, J. Hoefnagels, M. Geers, Microstructural study of the mechanical response of compacted graphite iron: An experimental and numerical approach, Mater. Sci. Eng., A 658 (2016) 439 – 449. doi:https://doi.org/10.1016/j.msea.2016.02.017.
URL http://www.sciencedirect.com/science/article/pii/S0921509316301319
[35] C. H. Scholz, Experimental study of the fracturing process in brittle rock, J. Geophys. Res. 73 (4) (1968) 1447–1454. arXiv:https://agupubs.onlinelibrary.wiley.com/doi/pdf/10.1029/JB073i004p01447, doi:10.1029/JB073i004p01447.
URL https://agupubs.onlinelibrary.wiley.com/doi/abs/10.1029/JB073i004p01447
[36] M. Barsoum, A. Murugaiah, S. Kalidindi, T. Zhen, Y. Gogotsi, Kink bands, nonlinear elasticity and nanoindentations in graphite, Carbon 42 (8) (2004) 1435 – 1445. doi:https://doi.org/10.1016/j.carbon.2003.12.090.
URL http://www.sciencedirect.com/science/article/pii/S000862230300678X
[37] D. E. Jiang, E. A. Carter, Carbon dissolution and diffusion in ferrite and austenite from first principles, Phys. Rev. B 67 (2003) 214103. doi:10.1103/PhysRevB.67.214103.
URL https://link.aps.org/doi/10.1103/PhysRevB.67.214103
[38] Y. Desplanques, G. Degallaix, R. Copin, Y. Berthier, A tribometer for the study of materials under railway braking conditions, in: G. Dalmaz, A. Lubrecht, D. Dowson, M. Priest (Eds.), Tribology Research: From Model Experiment to Industrial Problem, Vol. 39 of Tribology Series, Elsevier, 2001, pp. 381 – 391. doi:https://doi.org/10.1016/S0167-8922(01)80123-1.
URL http://www.sciencedirect.com/science/article/pii/S0167892201801231
[39] M. Kumar, J. Bijwe, Role of different metallic fillers in non-asbestos organic (nao) friction composites for controlling sensitivity of coefficient of friction to load and speed, Tribol. Int. 43 (5–6) (2010) 965 – 974, special Issue on Second International Conference on Advanced Tribology (iCAT2008). doi:http://dx.doi.org/10.1016/j.triboint.2009.12.062.
URL http://www.sciencedirect.com/science/article/pii/S0301679X09003995